

Macroscopic Manifestation of Domain-wall Magnetism and Magnetoelectric Effect in a Néel-type Skyrmion Host

K. Geirhos*,¹ B. Gross,² B. G. Szigeti,¹ A. Mehlin,² S. Philipp,² J. S. White,³ R. Cubitt,⁴ S. Widmann,¹ S. Ghara,¹ P. Lunkenheimer,¹ V. Tsurkan,^{1,5} A. O. Leonov,^{6,7} S. Bordács,^{8,9} M. Poggio,² and I. Kézsmárki¹

¹*Experimental Physics V, Center for Electronic Correlations and Magnetism,
University of Augsburg, 86135 Augsburg, Germany*

²*Department of Physics, University of Basel, 4056 Basel, Switzerland*

³*Laboratory for Neutron Scattering and Imaging,
Paul Scherrer Institut, CH-5232 Villigen, Switzerland*

⁴*Institut Laue-Langevin, 6 rue Jules Horowitz, 38042 Grenoble, France*

⁵*Institute of Applied Physics, Academy of Sciences of Moldova, MD 2028, Chisinau, Republica Moldova*

⁶*Center for Chiral Science, Hiroshima University, Higashi-Hiroshima, Hiroshima, 739-8526, Japan*

⁷*Department of Chemistry, Faculty of Science, Hiroshima University
Kagamiyama, Higashi-Hiroshima, Hiroshima, 739-8526, Japan*

⁸*Department of Physics, Budapest University of Technology and Economics, 1111 Budapest, Hungary*

⁹*Hungarian Academy of Sciences, Premium Postdoctor Program, 1051 Budapest, Hungary*

We report a magnetic state in GaV_4Se_8 which emerges exclusively in samples with mesoscale polar domains and not in polar mono-domain crystals. Its onset is accompanied with a sharp anomaly in the magnetic susceptibility and the magnetic torque, distinct from other anomalies observed also in polar mono-domain samples upon transitions between the cycloidal, the Néel-type skyrmion lattice and the ferromagnetic states. We ascribe this additional transition to the formation of magnetic textures localized at structural domain walls, where the magnetic interactions change stepwise and spin textures with different spiral planes, hosted by neighbouring domains, need to be matched. A clear anomaly in the magneto-current indicates that the domain-wall-confined magnetic states also have strong contributions to the magnetoelectric response. We expect polar domain walls to commonly host such confined magnetic edge states, especially in materials with long wavelength magnetic order.

Geometrical or dimensional constraints can promote the formation of new quantum phases which are absent in unconstrained bulk systems. Prominent examples include metallic surface states in topological insulators¹, superconducting vortex state below the Kosterlitz-Thouless transition², interface-induced 2D electron gas³ and superconductivity^{4–6}, integer and fractional quantum Hall edge states^{7–9} and Wigner crystals^{10,11} in systems with reduced dimensions. Geometrical constraints are usually enforced externally by synthesizing/structuring materials with mesoscopic dimensions, e.g., in the form of thin films, heterostructures, nanowires, quantum dots, etc. Such constraints can also emerge naturally via the formation of mesoscale structural domain patterns and topological defects^{12–19}.

Indeed, structural domain walls (DW) have recently been reported to possess novel functionalities, such as DW conductivity, electrical rectification and super switching, as observed in YMnO_3 ^{13,20}, ErMnO_3 ²¹, BiFeO_3 ^{16,22}, LiNbO_3 ²³, $\text{Pb}_x\text{Sr}_{1-x}\text{TiO}_3$ ²⁴, etc. Besides the peculiar electrical properties of DWs, the atomically sharp structural changes associated with them can substantially modify the magnetic exchange interactions and spin orders, as reported for $\text{SrRuO}_3\text{--Ca}_{0.5}\text{Sr}_{0.5}\text{TiO}_3$ heterostructures and thin films of $\text{La}_{2/3}\text{Sr}_{1/3}\text{MnO}_3$ and TbMnO_3 ^{19,25,26}. Furthermore, geometrical constraints were shown to substantially increase the thermal stability range of magnetic skyrmions^{27–29}, which are whirling spin textures on the nanoscale, and to generate exotic

magnetic edge states, such as chiral bobbles³⁰.

Lacunar spinels with the chemical formula AB_4X_8 ($\text{A} = \text{Al, Ga, Ge}$; $\text{B} = \text{V, Mo, Nb, Ta}$; $\text{X} = \text{S, Se, Te}$) are a family of narrow-gap Mott insulators, exhibiting a plethora of correlation and spin-orbit effects, including pressure-induced superconductivity³¹, bandwidth-controlled metal-to-insulator transition³², electric-field-driven avalanche of the Mott gap³³, large negative magnetoresistance³⁴, two-dimensional topological insulator state³⁵ and orbitally driven ferroelectricity^{36–39}. In addition to these charge related phenomena and particularly important for the present study, lacunar spinels, such as GaV_4S_8 , GaV_4Se_8 and GaMo_4S_8 , were the first material family found to host the Néel-type skyrmion lattice (SkL) state^{40–42}. In the last two compounds, the SkL state was reported to be stable down to zero Kelvin. While these materials have a cubic structure ($F\bar{4}3m$) at high temperature, many of them transform to a rhombohedral state ($R3m$) upon a Jahn-Teller transition, occurring around 30–50 K, which is triggered by the degeneracy of the B_4X_4 cluster orbitals^{37,43,44}. The polar axial symmetry of the low-temperature state is a prerequisite for the emergence of the Néel-type SkL state⁴⁵.

In this work, we demonstrate that non-trivial spin textures exist not only in the bulk, but complex magnetic states arise on the polar DWs of GaV_4Se_8 : The matching of spin cycloids at polar DWs gives rise to the emergence of a novel magnetic state confined to the DWs.

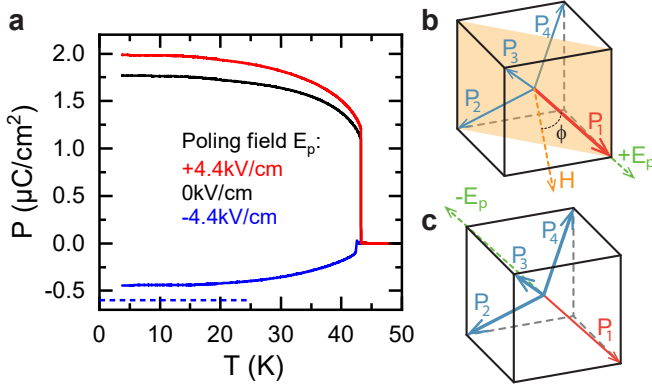


FIG. 1: Electric control of polar domains in GaV_4Se_8 . **a**, Temperature dependence of the polarization along the $[111]$ axis, measured during heating after poling with different electric fields, $E_p \parallel [111]$, upon cooling. The dashed line indicates the saturation polarization expected for negative poling fields. **b** & **c**, Schematic representations of the cubic unit cell indicating the four possible directions of the polarization, P_{1-4} , emerging in the rhombohedral phase. For $+E_p$, the unique P_1 domain is favored (**b**), for $-E_p$, the P_{2-4} domains are favored (**c**). In the magneto-current and torque experiments, described later, the magnetic field was rotated approximately in the $(1\bar{1}0)$ plane, highlighted in orange in panel **b**. The angle ϕ is spanned by the field and the $[111]$ axis.

Results

Electric control of polar domains.

In these compounds, four possible polar domains with polarizations along the cubic $\langle 111 \rangle$ -type axes can exist, that naturally form multi-domain, lamellar patterns. The DWs are $\{100\}$ -type planes with typical periodicity in the range of 10-1000 nm, as observed in GaV_4S_8 ¹⁸, GaV_4Se_8 ⁴⁶ and GaMo_4S_8 ⁴⁷ using atomic and piezoelectric force microscopy.

Besides the high DW density, another peculiarity of this polar phase is the lack of 180° DWs and the presence of 109° DWs only, owing to the non-centrosymmetric nature of the cubic phase^{18,47}. (This is in contrast to perovskite ferroelectrics, such as BiFeO_3 , where the paraelectric cubic phase is centrosymmetric.) Due to the lack of inversion domains, electric fields of opposite signs, applied along one of the four $\langle 111 \rangle$ -type axes, select either the unique domain with polarization parallel to the field or the other three domains, whose polarizations span 71° with the electric field. Such control of the polar domains in GaV_4Se_8 is sketched in Fig. 1 and also demonstrated via the temperature-dependent polarization, which was determined from pyrocurrent measurements, following electric-field poling. Indeed, the maximum polarization reached via positive electric fields ($2.0 \mu\text{C}/\text{cm}^2$) is considerably larger than for negative fields ($-0.45 \mu\text{C}/\text{cm}^2$). The ratio of the polarization values in the polar mono- and multi-domain states is expected to be 3:1 in the previous scenario, since the pyrocurrent component along

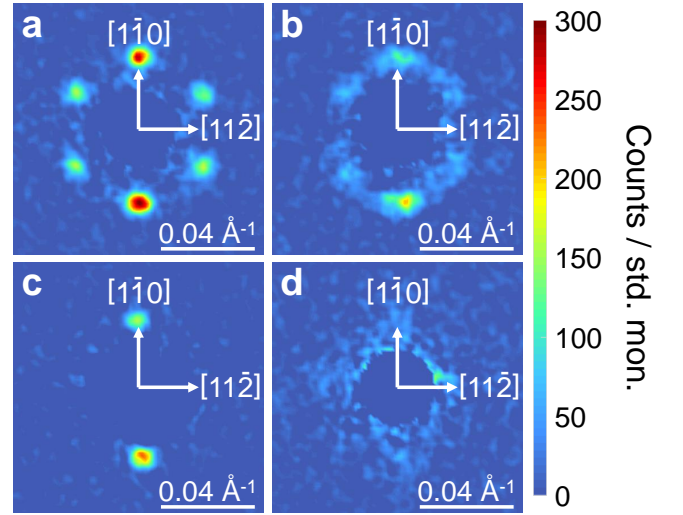


FIG. 2: Variation of the magnetic structure of GaV_4Se_8 in oblique magnetic fields. **a-d**, SANS images recorded at 12 K in 220 mT with the magnetic field spanning 0° , 21° , 27° and 35° with the $[111]$ axis, respectively. The hexagonal and the $\pm q$ patterns in panels **a** and **c** correspond to the SkL and cycloidal (conical) states, respectively. Panels **b** and **d** are images taken near the SkL→cycloidal and cycloidal→FM transitions, respectively.

the P_1 polar axis was detected.

Magnetic states in polar mono- and multi-domain GaV_4Se_8 crystals.

The different polar domains are also distinguished magnetically, since they are characterized by different directions of the uniaxial anisotropy, coinciding with the polar axes^{41,48,49}, and by different orientations of the Dzyaloshinskii-Moriya vectors that prefer modulated magnetic structures with q -vectors perpendicular to the polar axis. Correspondingly, for arbitrary directions of the magnetic field, distinct magnetic states can coexist on the different types of polar domains, as has been imaged in GaV_4S_8 by magnetic force microscopy⁴⁰. Furthermore, twisted magnetic textures confined to the vicinity of polar DWs have been observed in the same material¹⁸, though a systematic study of these edge states with changing the orientation of the field could not be performed.

Due to the uniaxial anisotropy of the material, the magnetic state depends not only on the magnitude, but also on the orientation of the field. A sequence of three different phases, SkL→cycloidal→ferromagnetic (FM), was observed at 12 K by small angle neutron scattering (SANS) while rotating a magnetic field of $\mu_0 H = 220 \text{ mT}$ in the $(1\bar{1}0)$ plane from the polar $[111]$ axis (H_\parallel) towards the perpendicular plane (H_\perp), as demonstrated in Fig. 2. The SANS patterns were recorded on the (111) plane for several angles of the field.

In order to continuously follow the phase boundaries on the H_\parallel - H_\perp plane, we carried out magneto-current and magnetic torque measurements, when the magnetic

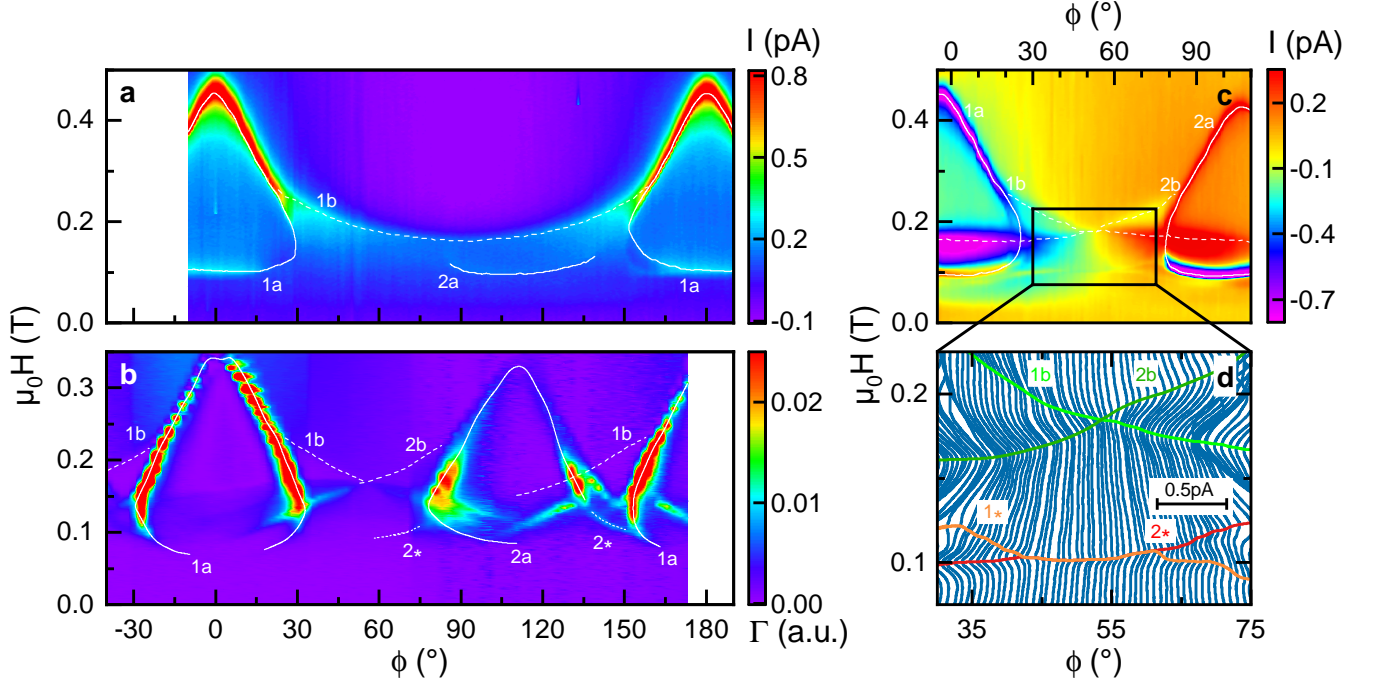


FIG. 3: Angular dependence of the magneto-current and the magnetic torque in GaV_4Se_8 at 12 K. Colour maps of **a** & **c**, the magneto-current and **b**, the dissipative part of the torque, as functions of the angle (ϕ) and the magnitude (H) of the magnetic field. Data shown in panel **a** were recorded on a nearly mono-domain sample, while data shown in panels **b** & **c** were obtained on polar multi-domain samples. Panel **d** shows a magnified view of the frame indicated in panel **c**, as a waterfall diagram, where the magneto-current curves recorded at different angles are shifted horizontally in proportion to ϕ . In each panel, the anomalies which can clearly be assigned to magnetic phase boundaries are highlighted by white lines and labeled, as follows. The numbers 1 and 2 correspond to domains with polar axes $[111]$ and $[\bar{1}\bar{1}1]$, respectively. The characters *a* and *b* correspond to the phase boundary of the SkL state (SkL-cycloidal and SkL-FM) and the cycloidal-FM boundary, respectively. The asterisks in panels **b** & **d** mark the newly found anomaly, associated with a magnetic transition within the DWs.

field was rotated in fine steps within the $(1\bar{1}0)$ plane between successive field sweeps. The corresponding data are depicted in Fig. 3 in the form of colour maps over the field magnitude-orientation plane (ϕ denotes the angle of the field spanned with the $[111]$ axis, as sketched in Fig. 1b), where the magnitude of the magneto-current (Figs. 3a & c) and the dissipative part of the torque signal (Fig. 3b) are represented by colours. The anomalies labeled in Fig. 3 are used to establish the magnetic phase diagrams corresponding to polar mono- and multi-domain samples in Figs. 4a & b, respectively, also supplemented with magnetization, susceptibility and SANS measurements. The phase boundaries determined from the torque measurements slightly deviate from those deduced by other methods, which is attributed to differences in the measurements conditions (sample temperature, sample orientation, direction of the field sweep, etc.). For a better match, the phase boundaries determined from torque measurements were plotted in Fig. 4a with H values rescaled by a factor of ~ 1.12 .

Fig. 3a shows magneto-current studies on a nearly polar mono-domain crystal, where all the observed anomalies (labeled as 1a and 1b) are assigned to transitions in

the P_1 domain with polar axis along the $[111]$ direction, except for a faint signal (labeled as 2a) in the angular range of 85° - 145° . The 180° periodicity of the signal can be readily followed. In contrast, Fig. 3b shows magnetic torque data as obtained on a polar multi-domain sample. Here, the faint feature, which is hardly traceable in the magneto-current data on the mono-domain sample, shows up clearly as a replica of the droplet-like motifs, which are the strong features centered around 0° and 180° in the nearly mono-domain sample. This additional droplet is also found in magneto-current studies on multi-domain samples, as shown in Fig. 3c. It is centered at around $\sim 109^\circ$, the angle spanned by the polar axes $[111]$ and $[\bar{1}\bar{1}1]$. Thus, it originates from the P_2 polar domain, whose polar axis also lies in the $(1\bar{1}0)$ rotation plane of the field. For multi-domain samples, the detailed angular dependence of the magneto-current and torque data reveal which magnetic anomalies can be assigned to P_1 or P_2 polar domains, and help to establish a domain-specific magnetic phase diagram (Fig. 4a), as if the samples were polar mono-domain. Magnetic anomalies corresponding to P_3 and P_4 domains cannot be unambiguously assigned, mainly because the angle spanned by the magnetic field

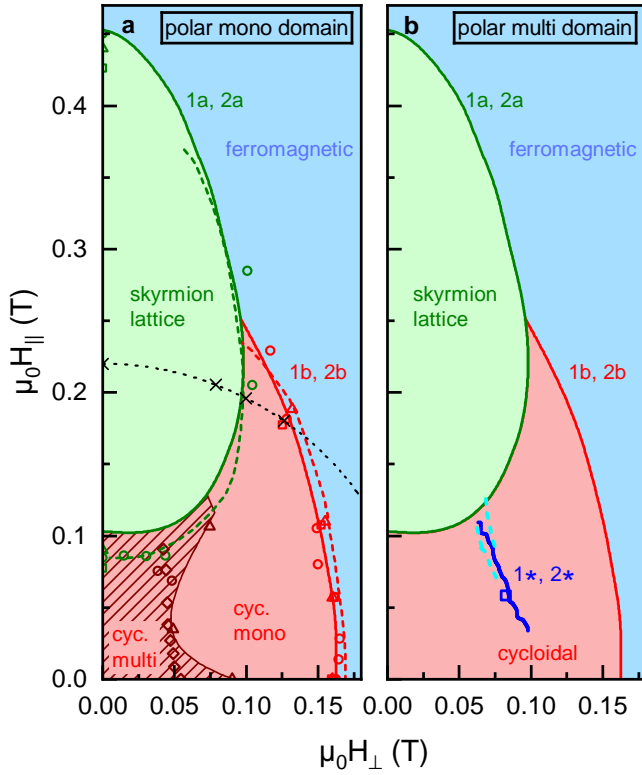


FIG. 4: Magnetic phase diagram representative to polar mono- and multi-domain GaV_4Se_8 crystals at 12 K, displayed in panel a & b, respectively. The solid and dashed lines are phase boundaries deduced from magneto-current and torque measurements, respectively. Triangles represent SANS data, while circles/squares correspond to magnetization measurements without/with electric field poling. Note that panel **a** does not exclusively contain data obtained on polar mono-domain samples, but includes all anomalies, which are present irrespective if the samples are mono- or multi-domain ones. In case of polar multi-domain crystals, H_{\parallel} and H_{\perp} refers to field components parallel and perpendicular to the polar axis of the domain to which the anomalies are assigned. For the assignment of the different anomalies to different polar domains in multi-domain crystals and the establishment of the unified phase diagram, see the main text. The hashed low-field area in panel **a** indicates the region of the cycloidal q-vector reorientation, while the black crosses along the dashed black line correspond to the points where the SANS images in Fig. 2 were taken. In panel **b**, the phase boundaries, which are also present in the polar mono-domain case, are shown only as deduced from the magneto-current measurements. Labels of the phase boundaries ($1a$, $1b$, $2a$, $2b$) correspond to those in Fig. 3. The additional phase boundary labeled by 1^* & 2^* is determined by magneto-current (solid blue line), by torque (dashed light blue line) and by susceptibility measurements (blue square).

and their polar axes varies over a limited range, $54-90^\circ$, while the field is rotated in the $(1\bar{1}0)$ plane.

In polar mono-domain samples (Fig. 4a), there are three magnetic phases showing up, the cycloidal, the Néel-type SkL and the FM state, in accord with for-

mer studies^{41,50}. Note that phase boundaries in Fig. 4a are displayed from one hand, as obtained from magneto-current data on a nearly polar mono-domain crystal (Fig. 3a). On the other hand, Fig. 4a also shows how the phase diagram looks like for a given domain in a polar multi-domain crystal, when the orientation of the field is measured from the polar axis of that domain. Since there is no difference between the two cases, phase boundaries in Fig. 4a are representative to the magnetic states inside the polar domains. In fields applied along the polar axis, the cycloidal phase has coexisting domains with wavevectors oriented in different directions (in the plane perpendicular to the rhombohedral axis) up to its transformation to the SkL state^{40,41}. By oblique fields, this cycloidal multi-domain state is turned to a cycloidal mono-domain state, since H_{\perp} selects the unique q-vector, which is perpendicular to this field component⁴¹. This repopulation of the cycloidal domains is directly detected by SANS experiments (see Fig. S1 in the Supplemental material) and also manifested in magnetic susceptibility and magneto-current data as a low-field upturn and a peak, respectively, at $H_{\perp} \sim 40 \text{ mT}$, as discerned e.g. in Figs. 5a & b. (For details see Fig. S2 in the Supplemental material.) The crossover regime from the cycloidal multi-to mono-domain state is also indicated in Fig. 4a. Another important observation is that for certain angles of oblique fields, there is a re-entrant cycloidal state, where the full sequence of magnetic transitions with increasing field is cycloidal \rightarrow SkL \rightarrow cycloidal \rightarrow FM. This re-entrance of the cycloidal phase, found in magnetization, magneto-current and torque experiments for $\phi = 21 - 29^\circ$, has been predicted for oblique fields in GaV_4Se_8 ⁵¹, but has not been observed yet^{41,50}.

In polar multi-domain samples, besides the features assigned to magnetic transitions within the bulk of the different polar domains, there are additional anomalies in the torque and magneto-current data, marked by asterisks in Figs. 3b & d, respectively. In case of magneto-current measurements, the corresponding angular range ($\phi = 30-75^\circ$) is highlighted by a rectangle in Fig. 3c and a zoom-in view of the magneto-current curves is given in Fig. 3d. In the torque data, there are additional weak features observed⁵². However, here we only discuss anomalies simultaneously discerned in magnetization, magneto-current and torque data.

The key observation of the present work is the emergence of this additional magnetic transition in polar multi-domain samples, as shown in Fig. 4b. This change in the magnetic state is triggered by oblique fields and located in the middle of the cycloidal phase, where the cycloidal modulation with a unique q-vector is already established by the H_{\perp} component of the field. Fig. 5 summarizes the signatures of this extra transition, based on various quantities measured in $\mathbf{H} \parallel [001]$. This choice of the field orientation guarantees that all the polar domains host the same magnetic state, irrespective of the magnitude of the field, since the $[001]$ axis spans the same angle (54°) with the magnetic anisotropy axes of all the four

polar domains. Thus, one would expect the same magnetic anomalies, irrespective of having a polar mono- or multi-domain sample, unless the presence of DWs introduces an additional magnetic state not existing inside the domains. The magnetic susceptibility has a sharp peak at ~ 100 mT for the polar multi-domain sample, which is strongly suppressed as the polar mono-domain state is approached, but not fully achieved by poling. The poling worked more efficiently for the thin platelet used in the magneto-current studies: The sharp step in the magneto-current curve associated with this transition is completely suppressed, as the polar mono-domain state is reached. The dissipative part of the magnetic torque signal also shows a weak anomaly at this field, though it is better visible a few degrees away from the $[001]$ direction. In this case the mono-domain state could not be studied due to the unfeasibility of electric poling. In the field dependence of the SANS intensity we could not observe any anomaly associated with this transition. This may be due to the signal to noise ratio and the limited field resolution in the SANS measurements.

Another observation supporting that the new anomaly is associated with magnetic states confined to the vicinity of DWs and not extended over the entire volume of the crystals is the weakness of the anomaly in the magnetic properties. Namely, the magnitude of the step-wise increase in the magnetization, corresponding to the susceptibility peak observed at 100 mT with $\mathbf{H} \parallel [001]$, is less than 5% of the magnetization step observed upon the cycloidal to SkL transition in similar fields for $\mathbf{H} \parallel [111]$. (See Fig. S3 in the Supplemental material.) Another possibility would be that while the anomaly is readily linked to the presence of DWs, as demonstrated by electric poling experiments, it is associated to a novel magnetic state triggered by the DWs but not confined to their vicinity. However, in this case the critical field of the corresponding transition would depend on the distance of neighbouring DWs and, therefore, should show a broad distribution. In contrast, the observed anomaly is rather sharp with a full width of $\lesssim 3$ mT.

Discussion

Our study demonstrates that the existence of DWs is a prerequisite for the emergence of the new magnetic state in GaV_4Se_8 , as revealed by macroscopic magnetic and magnetoelectric properties. The density of DWs is rather high in this compound⁴⁶, especially if we compare the typical DW distance of ~ 100 -200 nm to the wavelength of the Néel-type magnetic modulations of ~ 20 nm. The DWs separating polar rhombohedral domains in this compound do not only produce a sudden change in the direction of the magnetic anisotropy axis but also change the orientation of the Dzyaloshinskii-Moriya vectors. We think that the mismatch between different modulated states, favoured by different magnetic interactions at adjacent domains, can give rise to the formation of new

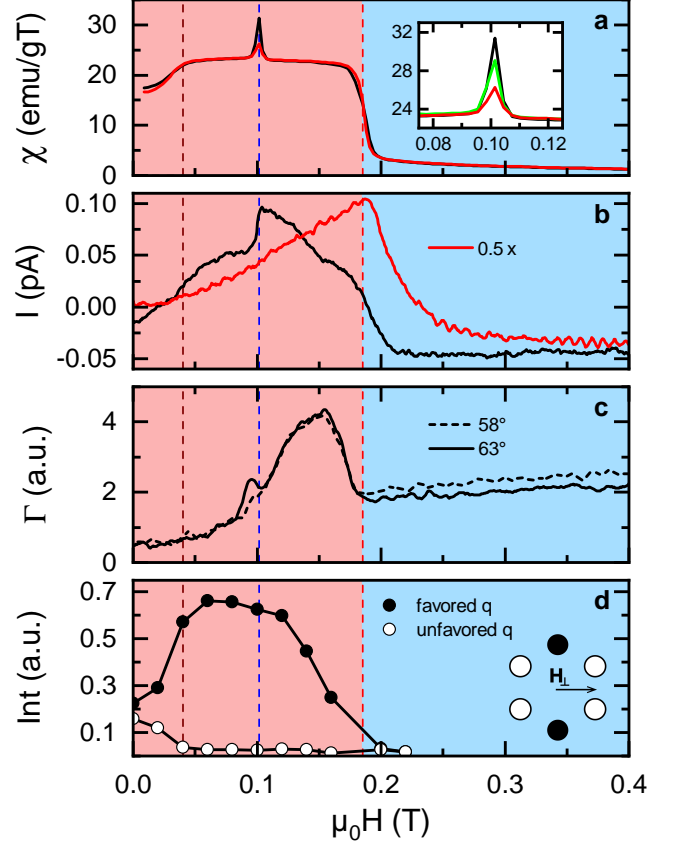


FIG. 5: Magnetic anomalies in polar mono- and multi-domain GaV_4Se_8 crystals at 12 K. Magnetic field dependence of **a**, the real part of the ac-susceptibility, **b**, the magneto-current, **c**, the dissipative part of the torque and **d**, the SANS intensity, all measured in $\mathbf{H} \parallel [001]$ ($\phi \sim 54^\circ$). Curves displayed in black/red were recorded on polar multi-/mono-domain crystals. The inset in panel **a** shows a magnified view of the anomaly around 100 mT for three different electric poling fields (red: $+2.5 \frac{\text{kV}}{\text{cm}}$, green: $0 \frac{\text{kV}}{\text{cm}}$, black: $-2.5 \frac{\text{kV}}{\text{cm}}$). The brown, blue and red vertical dashed lines indicate the q-vector re-orientation, the anomaly observed in multi-domain samples and the cycloidal \rightarrow FM transition, respectively.

spin textures at the DWs. We expect that the new magnetic state conned to DWs transforms to the FM state at the same time as the cycloidal to FM transition happens inside the domains. This is in accord with the lack of a second weak anomaly in Fig. 4b, based on the magnetization, torque and magneto-current data for polar multi-domain samples. An alternative scenario is that the magnetic frustration coming from the change of the Dzyaloshinskii-Moriya interaction at DWs may also suppress the stability range of the modulated states near the DWs, since the critical magnetic field, where the modulated states transform to the FM state, scales with D^2/J , where D is the strength of the Dzyaloshinskii-Moriya interaction and J is the isotropic Heisenberg exchange. The corresponding scenario for the magnetic anomaly,

observed exclusively in polar multi-domain samples, is that the DW region becomes FM at lower fields, when the cycloidal modulations still persist inside the domains.

It is important to note that the two transition lines 1* and 2* in Figs. 3c & d fall on each other and form a single phase boundary in Fig. 4b, if they are respectively assigned to P_1 and P_2 domains, meaning that the angle of the magnetic field is measured from the corresponding polar axes. From this, we conclude that these conjoined magnetic states do not form on DWs between P_1 and P_2 domains, but on $P_1 - P_3$ or $P_2 - P_4$ DWs parallel to the (100) plane or on $P_1 - P_4$ or $P_2 - P_3$ DWs parallel to the (010) plane. As discussed earlier, the magnetic anisotropy axis of each domain spans the same angle with the field for $\mathbf{H} \parallel [001]$, thus, the same magnetic state exists inside all the domains. In contrast, not all the DWs are magnetically equivalent for this specific field orientation: $\mathbf{H} \parallel [001]$ lies within the plane of the four types of DWs listed above and is perpendicular to the $P_1 - P_2$ and $P_3 - P_4$ DWs. (For details, see Fig. S4 in the Supplemental material.) Note that in the angular range, where the new state appears at the DWs, the corresponding domains host the cycloidal state. Consequently, the edge state emerges due to the imperfect matching of two cycloids with different rotation planes. A similar phenomenon has recently been observed for antiferromagnetic spin cycloids interfaced at polar DWs of BiFeO_3 ^{53,54}. More specific information about the nature of the new magnetic state would require the real-space imaging of magnetic textures in GaV_4Se_8 . Such trials on GaV_4Se_8 have not been successful so far, in contrast to GaV_4S_8 , where we could even observe magnetic textures localized to DWs¹⁸ besides the extended cycloidal and SkL states⁴⁰.

Recently, the influence of structural DWs on macroscopic (bulk) electronic properties has been extensively investigated^{20,23}. In contrast, manifestations of spin textures confined to DWs in macroscopic magnetic properties have hardly been observed. In the present work, we found sharp magnetic and magnetoelectric anomalies in GaV_4Se_8 what we assign to a phase transition originating from magnetic states confined to the vicinity of structural DWs.

Methods

Sample synthesis and characterization. Single crystals of GaV_4Se_8 with typical mass of 1-30 mg were grown by the chemical vapour transport method using iodine as the transport agent. The crystallographic orientation of the samples was determined by X-ray Laue and neutron diffraction.

Magnetization measurements. The magnetization and ac susceptibility measurements were performed following an initial zero-field cooling, using an Magnetic Property Measurement System (MPMS) from Quantum Design. For ac susceptibility measurements with electric

field poling, a home made probe was used. Poling electric field was applied only during cooling.

Magneto-current measurements. For the pyro- and magneto-current measurements, contacts on two parallel (111) faces of the crystals were applied using silver paint. The sample was cooled using an Oxford helium flow cryostat. For changing the orientation of the magnetic field with respect to the electric contacts, the sample was mounted on a platform, which can be rotated by a stepper motor. To ensure low noise measurements, the platform was equipped with two coaxial cables. For magneto-current measurements, the current was recorded using Keysight B2987A electrometer while the magnetic field was swept with a typical rate of 0.5-1 T/min. For pyrocurrent measurements, the current was recorded with the same electrometer while the temperature was swept from 3 K to 50 K with a rate of about 6 K/min.

Torque magnetometry. Torque data was recorded with dynamic cantilever magnetometry (DCM)^{29,55}. A single crystalline piece of GaV_4Se_8 (spatial dimensions in the order of 100 μm) was attached to the end of a commercial cantilever (Arrow-TL1, Nanoworld). In DCM, the cantilever is driven into self-oscillation at its resonance frequency. Changes in the dissipation $\Delta\Gamma = \Gamma - \Gamma_0$, induced by the torque from the sample, are measured as a function of the uniform applied magnetic field \mathbf{H} , where Γ_0 is the cantilever's intrinsic mechanical dissipation at $H = 0$. Measurements of $\Delta\Gamma$ are particularly useful for identifying magnetic phase transitions²⁹.

DCM measurements were carried out in a vibration-isolated closed-cycle cryostat. The pressure in the sample chamber is less than 10^{-6} mbar and the temperature can be stabilized between 4-300 K. Using an external rotatable superconducting magnet, magnetic fields up to 4.5 T can be applied along any direction spanning 120° in the plane of cantilever oscillation. A piezoelectric actuator mechanically drives the cantilever with a constant oscillation amplitude of a few tens of nanometers using a feedback loop implemented by a field-programmable gate array. The cantilever's motion is read out using an optical fiber interferometer using 100 nW of laser light at 1550 nm⁵⁶.

Small-angle neutron scattering. Small-angle neutron scattering (SANS) was performed on a 11.6 mg single crystal sample of GaV_4Se_8 . SANS patterns discussed in the main text were measured using the SANS-I instrument of SINQ at the Paul Scherrer Institut (PSI), Villigen, Switzerland. The wavelength of the incoming neutrons was 6 \AA , the collimation and the sample-detector distances were set to 6 m. The magnetic field was applied in various directions within the (1 $\bar{1}$ 0) plane. Additionally, magnetic field dependence of the scattering data shown in the supplement was measured using the D11 and the D33 instruments at the Institut Laue-Langevin (ILL), Grenoble, France. The neutron wavelength of 5 \AA was selected and the collimator-sample and the sample-detector distances were set to 5 m. In all experiments the sample to-

gether with the magnet is rotated and tilted, i.e. rocked in order to move the magnetic diffraction peaks through the Ewald sphere. The SANS patterns presented are the sum of intensities through the whole rocking angle range. Similar measurements were taken in the paramagnetic phase at 20 K, and subtracted from the data to obtain the magnetic scattering data.

Data Availability

The measurement data from ILL is publicly available under the ILL DOI-s <https://doi.ill.fr/10.5291/ILL-DATA.INTER-338> and <https://doi.ill.fr/10.5291/ILL-DATA.5-42-438>. The rest of the data that support the findings of this study are available from the corresponding author upon reasonable request.

Bibliography

- ¹ Hasan, M. Z. & Kane, C. L. Colloquium: Topological insulators. *Rev. Mod. Phys.* **82**, 3045–3067 (2010).
- ² Resnick, D. J., Garland, J. C., Boyd, J. T., Shoemaker, S. & Newrock, R. S. Kosterlitz-Thouless transition in proximity-coupled superconducting arrays. *Phys. Rev. Lett.* **47**, 1542–1545 (1981).
- ³ Ohtomo, A. & Hwang, H. Y. A high-mobility electron gas at the $\text{LaAlO}_3/\text{SrTiO}_3$ heterointerface. *Nature* **427**, 423–426 (2004).
- ⁴ Wang, Q.-Y. *et al.* Interface-induced high-temperature superconductivity in single unit-cell FeSe films on SrTiO_3 . *Chinese Phys. Lett.* **29**, 037402–037405 (2012).
- ⁵ He, S. *et al.* Phase diagram and electronic indication of high-temperature superconductivity at 65 K in single-layer FeSe films. *Nat. Mater.* **12**, 605–610 (2013).
- ⁶ Reyren, N. *et al.* Superconducting interfaces between insulating oxides. *Science* **317**, 1196–1199 (2007).
- ⁷ Nakamura, J. *et al.* Aharonov–Bohm interference of fractional quantum Hall edge modes. *Nat. Phys.* **15**, 563–569 (2019).
- ⁸ Cohen, Y. *et al.* Synthesizing a $\nu = 2/3$ fractional quantum Hall effect edge state from counter-propagating $\nu = 1$ and $\nu = 1/3$ states. *Nat. Commun.* **10**, 1920–1925 (2019).
- ⁹ MacDonald, A. H. Edge states in the fractional-quantum-Hall-effect regime. *Phys. Rev. Lett.* **64**, 220–223 (1990).
- ¹⁰ Andrei, E. Y. *et al.* Observation of a magnetically induced Wigner solid. *Phys. Rev. Lett.* **60**, 2765–2768 (1988).
- ¹¹ Shapir, I. *et al.* Imaging the electronic Wigner crystal in one dimension. *Science* **364**, 870–875 (2019).
- ¹² Zurek, W. H. Cosmological experiments in superfluid helium? *Nature* **317**, 505–508 (1985).
- ¹³ Choi, T. *et al.* Insulating interlocked ferroelectric and structural antiphase domain walls in multiferroic YMnO_3 . *Nat. Mater.* **9**, 253–258 (2010).
- ¹⁴ Chae, S. C. *et al.* Self-organization, condensation, and annihilation of topological vortices and antivortices in a multiferroic. *P. Natl. Acad. Sci. USA* **107**, 21366–21370 (2010).
- ¹⁵ Lilienblum, M. *et al.* Ferroelectricity in the multiferroic hexagonal manganites. *Nat. Phys.* **11**, 1070–1073 (2015).
- ¹⁶ Ma, J. *et al.* Controllable conductive readout in self-assembled, topologically confined ferroelectric domain walls. *Nat. Nanotechnol.* **13**, 947–952 (2018).
- ¹⁷ Seidel, J. *Topological Structures in Ferroic Materials* (Springer, New York City, 2016).
- ¹⁸ Butykai, Á. *et al.* Characteristics of ferroelectric-ferroelastic domains in Néel-type skyrmion host GaV_4S_8 . *Sci. Rep.* **7**, 44663–44674 (2017).
- ¹⁹ Farokhipoor, S. *et al.* Artificial chemical and magnetic structure at the domain walls of an epitaxial oxide. *Nature* **515**, 379–383 (2014).
- ²⁰ Ruff, E. *et al.* Conductivity contrast and tunneling charge transport in the vortexlike ferroelectric domain patterns of multiferroic hexagonal YMnO_3 . *Phys. Rev. Lett.* **118**, 036803–036807 (2017).
- ²¹ Schaab, J. *et al.* Electrical half-wave rectification at ferroelectric domain walls. *Nat. Nanotechnol.* **13**, 1028–1034 (2018).
- ²² Seidel, J. *et al.* Conduction at domain walls in oxide multiferroics. *Nat. Mater.* **8**, 229–234 (2009).
- ²³ Werner, C. S. *et al.* Large and accessible conductivity of charged domain walls in lithium niobate. *Sci. Rep.* **7**, 9862–9869 (2017).
- ²⁴ Matzen, S. *et al.* Super switching and control of in-plane ferroelectric nanodomains in strained thin films. *Nat. Commun.* **5**, 4415–4422 (2014).
- ²⁵ Kan, D. *et al.* Tuning magnetic anisotropy by interfacially engineering the oxygen coordination environment in a transition metal oxide. *Nat. Mater.* **15**, 432–437 (2016).
- ²⁶ Liao, Z. *et al.* Controlled lateral anisotropy in correlated manganite heterostructures by interface-engineered oxygen octahedral coupling. *Nat. Mater.* **15**, 425–431 (2016).
- ²⁷ Yu, X. Z. *et al.* Near room-temperature formation of a skyrmion crystal in thin-films of the helimagnet FeGe . *Nat. Mater.* **10**, 106–109 (2011).
- ²⁸ Sonntag, A., Hermenau, J., Krause, S. & Wiesendanger, R. Thermal stability of an interface-stabilized skyrmion lattice. *Phys. Rev. Lett.* **113**, 077202–077205 (2014).
- ²⁹ Mehlin, A. *et al.* Stabilized skyrmion phase detected in MnSi nanowires by dynamic cantilever magnetometry. *Nano Lett.* **15**, 4839–4844 (2015).
- ³⁰ Zheng, F. *et al.* Experimental observation of chiral magnetic bobbles in B20-type FeGe . *Nat. Nanotechnol.* **13**, 451–455 (2018).
- ³¹ Abd-Elmeguid, M. M. *et al.* Transition from Mott insulator to superconductor in GaNb_4Se_8 and GaTa_4Se_8 under high pressure. *Phys. Rev. Lett.* **93**, 126403–126406 (2004).
- ³² Phuoc, V. T. *et al.* Optical conductivity measurements of GaTa_4Se_8 under high pressure: Evidence of a bandwidth-controlled insulator-to-metal Mott transition. *Phys. Rev. Lett.* **110**, 037401–037405 (2013).
- ³³ Guiot, V. *et al.* Avalanche breakdown in $\text{GaTa}_4\text{Se}_{8-x}\text{Te}_x$ narrow-gap Mott insulators. *Nat. Commun.* **4**, 1722–1727 (2013).
- ³⁴ Dorolti, E. *et al.* Half-metallic ferromagnetism and large negative magnetoresistance in the new lacunar spinel GaTi_3VS_8 . *J. Am. Chem. Soc.* **132**, 5704–5710 (2010).
- ³⁵ Kim, H.-S., Im, J., Han, M. J. & Jin, H. Spin-orbital entangled molecular j_{eff} states in lacunar spinel compounds. *Nat. Commun.* **5**, 3988–3994 (2014).
- ³⁶ Singh, K. *et al.* Orbital-ordering-driven multiferroicity and magnetoelectric coupling in GeV_4S_8 . *Phys. Rev. Lett.* **113**, 137602–137606 (2014).

- ³⁷ Wang, Z. *et al.* Polar dynamics at the Jahn-Teller transition in ferroelectric GaV_4S_8 . *Phys. Rev. Lett.* **115**, 207601–207605 (2015).
- ³⁸ Geirhos, K. *et al.* Orbital-order driven ferroelectricity and dipolar relaxation dynamics in multiferroic GaMo_4S_8 . *Phys. Rev. B*. **98**, 224306–224311 (2018).
- ³⁹ Ruff, E. *et al.* Polar and magnetic order in GaV_4S_8 . *Phys. Rev. B*. **96**, 165119–165125 (2017).
- ⁴⁰ Kézsmárki, I. *et al.* Néel-type skyrmion lattice with confined orientation in the polar magnetic semiconductor GaV_4S_8 . *Nat. Mater.* **14**, 1116–1122 (2015).
- ⁴¹ Bordács, S. *et al.* Equilibrium skyrmion lattice ground state in a polar easy-plane magnet. *Sci. Rep.* **7**, 7584–7594 (2017).
- ⁴² Butykai, Á. *et al.* Squeezing magnetic modulations by enhanced spin-orbit coupling of 4d electrons in the polar semiconductor GaMo_4S_8 . *arXiv* (2019).
- ⁴³ Pocha, R., Johrendt, D. & Pöttgen, R. Electronic and structural instabilities in GaV_4S_8 and GaMo_4S_8 . *Chem. Mater.* **12**, 2882–2887 (2000).
- ⁴⁴ Hlinka, J. *et al.* Lattice modes and the Jahn-Teller ferroelectric transition of GaV_4S_8 . *Phys. Rev. B*. **94**, 060104–060108 (2016).
- ⁴⁵ Bogdanov, A. N. & Yablonskii, D. A. Thermodynamically stable "vortices" in magnetically ordered crystals. The mixed state of magnets. *Zh. Eksp. Teor. Fiz.* **95**, 178–180 (1989).
- ⁴⁶ Milde, P. Unpublished (2020).
- ⁴⁷ Neuber, E. *et al.* Architecture of nanoscale ferroelectric domains in GaMo_4S_8 . *J. Phys.-Condens. Mat.* **30**, 445402–445411 (2018).
- ⁴⁸ Ehlers, D. *et al.* Exchange anisotropy in the skyrmion host GaV_4S_8 . *J. Phys.-Condens. Mat.* **29**, 065803–065811 (2017).
- ⁴⁹ Ehlers, D. *et al.* Skyrmion dynamics under uniaxial anisotropy. *Phys. Rev. B*. **94**, 014406–014411 (2016).
- ⁵⁰ Fujima, Y., Abe, N., Tokunaga, Y. & Arima, T. Thermodynamically stable skyrmion lattice at low temperatures in a bulk crystal of lacunar spinel GaV_4S_8 . *Phys. Rev. B*. **95**, 180410–180414 (2017).
- ⁵¹ Leonov, A. O. & Kézsmárki, I. Skyrmion robustness in noncentrosymmetric magnets with axial symmetry: The role of anisotropy and tilted magnetic fields. *Phys. Rev. B*. **96**, 214413–214421 (2017).
- ⁵² Poggio, M. Unpublished (2020).
- ⁵³ Chauleau, J.-Y. *et al.* Electric and antiferromagnetic chiral textures at multiferroic domain walls. *Nat. Mater.* 1–5 (2019).
- ⁵⁴ Xue, F., Yang, T. & Chen, L.-Q. Electric-field-induced switching dynamics of cycloidal spins in multiferroic BiFeO_3 : phase-field simulations. *arXiv* (2019).
- ⁵⁵ Gross, B. *et al.* Dynamic cantilever magnetometry of individual CoFeB nanotubes. *Phys. Rev. B*. **93**, 064409–064423 (2016).
- ⁵⁶ Rugar, D., Mamin, H. J. & Guethner, P. Improved fiber-optic interferometer for atomic force microscopy. *Appl. Phys. Lett.* **55**, 2588–2590 (1989).

Acknowledgements We thank Á. Butykai for stimulating discussions. This work was supported by the DFG via the Transregional Research Collaboration TRR 80 From Electronic Correlations to Functionality (Augsburg/Munich/Stuttgart), by the Hungarian National Research, Development and Innovation Office NKFIH, ANN 122879 BME-Nanonotechnology FIKP grant (BME FIKP-NAT), by the Swiss National Science Foundation via Grants No. 200020-159893, the Sinergia network Nanoskyrmionics (Grant No. CRSII5-171003), and the NCCR Quantum Science and Technology (QSIT).

Author Contributions V.T. synthesized the crystals; B.G., A.M., S.P., M.P. performed and analysed the torque measurements; K.G., P.L. performed and analysed the pyro- and magneto-current measurements; B.G.Sz., S.B., J.S.W., R.C., I.K. performed and analysed the SANS measurements; S.G., S.W. performed and analysed the magnetization measurements; I.K. wrote the manuscript; I.K., M.P., S.B. planned the project.

Competing interests The authors declare no competing financial interests.

Additional information Supplementary Information is available for this paper. Correspondence and requests for materials should be addressed to K. G.. Reprints and permissions information is available at www.nature.com/reprints.